Title

Discovery of active off-axis hydrothermal vents at 9° 54′N East Pacific Rise

Journal

Proceedings of the National Academy of Sciences of the United States of America, 119(30)

ISSN

0027-8424

Authors

McDermott, Jill M
Parnell-Turner, Ross
Barreyre, Thibaut
et al.

Publication Date

2022-07-26

DOI

10.1073/pnas.2205602119

PNAS RESEARCH ARTICLE | EARTH, ATMOSPHERIC, AND PLANETARY SCIENCES

Discovery of active off-axis hydrothermal vents at 9° 54′N East Pacific Rise

Jill M. McDermott[a,1], Ross Parnell-Turner[b], Thibaut Barreyre[c], Santiago Herrera[d], Connor C. Downing[a], Nicole C. Pittoors[d], Kelden Pehr[a], Samuel A. Vohsen[d], William S. Dowd[a], Jyun-Nai Wu[b], Milena Marjanović[e], and Daniel J. Fornari[f]

Edited by Michael Manga, University of California, Berkeley, CA; received March 30, 2022; accepted June 7, 2022

Comprehensive knowledge of the distribution of active hydrothermal vent fields along midocean ridges is essential to understanding global chemical and heat fluxes and endemic faunal distributions. However, current knowledge is biased by a historical preference for on-axis surveys. A scarcity of high-resolution bathymetric surveys in off-axis regions limits vent identification, which implies that the number of vents may be underestimated. Here, we present the discovery of an active, high-temperature, off-axis hydrothermal field on a fast-spreading ridge. The vent field is located 750 m east of the East Pacific Rise axis and ∼7 km north of on-axis vents at 9° 50′N, which are situated in a 50- to 100-m-wide trough. This site is currently the largest vent field known on the East Pacific Rise between 9 and 10° N. Its proximity to a normal fault suggests that hydrothermal fluid pathways are tectonically controlled. Geochemical evidence reveals deep fluid circulation to depths only 160 m above the axial magma lens. Relative to on-axis vents at 9° 50′N, these off-axis fluids attain higher temperatures and pressures. This tectonically controlled vent field may therefore exhibit greater stability in fluid composition, in contrast to more dynamic, dike-controlled, on-axis vents. The location of this site indicates that high-temperature convective circulation cells extend to greater distances off axis than previously realized. Thorough high-resolution mapping is necessary to understand the distribution, frequency, and physical controls on active off-axis vent fields so that their contribution to global heat and chemical fluxes and role in metacommunity dynamics can be determined.

hydrothermal activity | midocean ridge | ocean chemistry | chemosynthetic ecosystem | East Pacific Rise

Significance

We describe the discovery of a large, active, high-temperature off-axis hydrothermal vent field on the East Pacific Rise. Hydrothermal vents are more prevalent across the crestal region of midocean ridges than previously thought. Our finding has important implications for understanding the fundamental controls on vent location and hydrology of hydrothermal systems along the crest of fast-spreading midocean ridges. The site provides a validation point for observations and models that call for significant hydrothermal heat loss beyond the immediate spreading axis. Finding an active off-axis vent field implies that temporally stable off-axis vent-endemic populations may provide a source of colonizing fauna to on-axis hydrothermal ecosystems after seafloor volcanic eruptions.

The circulation of high-temperature hydrothermal fluids through the global midocean ridge (MOR) system plays a central role in mediating global seawater chemistry on short and long timescales (1). Fluid–mineral reactions in hydrothermal systems result in secondary mineral formation and chemical exchange between seawater and the oceanic crust. At the same time, fluid–seawater mixing generates biogeochemical gradients that support chemosynthetic life (2, 3). Quantifying total hydrothermal chemical and heat fluxes from MOR vent sources into the global ocean is a persistent and complex problem. Understanding variability in vent fluid exit temperature and chemistry across different tectonic and magmatic regimes continues to be a key research objective in oceanography.

The spatial distribution of known vent fields forms the basis for understanding global chemical and heat fluxes. Since their first discovery near 21° N in 1979 (4), active hydrothermal vent fields on the intermediate- to fast-spreading East Pacific Rise (EPR) have always been found within a few hundred meters of the ∼50- to 200-m-wide graben that marks the plate boundary (5), called the axial summit trough (AST). Vent fields on the EPR were found only along fissures within the AST floor or on its steep-sided bounding walls (6). Along the EPR, hydrothermal vent fields commonly occur on the shallowest segments of the ridge axis, in regions associated with zones of robust, shallow magma storage and supply (7, 8). However, these observations are biased due to a historical preference for on-axis MOR field studies.

The lack of systematic surveying of off-axis regions via either plume surveys or mapping at sufficient resolution (i.e., 1- to 2-m pixels) to identify potential vent fields is a first-order limitation to quantifying hydrothermal chemical and heat fluxes. Long-standing questions remain regarding the mechanisms of heat extraction from young oceanic crust. A geochemical study of the sheeted dikes cored at Integrated Ocean Drilling Program Hole 1256D argues that focused fluid flow along faults could reconcile near-axis heat loss budgets (9). Indeed, hydrothermal deposits have been documented at fault scarps on two abyssal hills near the EPR. One deposit is ∼5 km east of the axis at 10° 20′N, 103° 33.2′W, and the other deposit is ∼26 km west of the axis at 9° 27′N, 104° 32.3′W and is associated with diffuse fluids (10). Combined, those observations

Author contributions: J.M.M., R.P.-T., T.B., and D.J.F. designed research; J.M.M., R.P.-T., T.B., S.H., C.C.D., N.C.P., K.P., S.A.V., W.S.D., J.-N.W., M.M., and D.J.F. performed research; J.M.M., R.P.-T., T.B., S.H., N.P., M.M., and D.J.F. analyzed data; and J.M.M., R.P.-T., T.B., S.H., C.C.D., N.C.P., K.P., S.A.V., W.S.D., J.-N.W., M.M., and D.J.F. wrote the paper.

The authors declare no competing interest.

This article is a PNAS Direct Submission.

See online for related content such as Commentaries.

[1]To whom correspondence may be addressed. Email: jill.mcdermott@lehigh.edu.

This article contains supporting information online at http://www.pnas.org/lookup/suppl/doi:10.1073/pnas.2205602119/-/DCSupplemental.

Published July 21, 2022.

demonstrated that fault-driven fluid flow can occur off axis, yet the distances over which high-temperature convective circulation cells extend off axis remain largely unknown. Understanding the spatial distribution of hydrothermal sources is important to determining the ratio of conductive to convective heat loss, along and across the global ridge crest in modern (11) and paleo (12) ocean basins. This understanding is also relevant to accretionary processes that build the ocean crust at the plate boundary (13, 14).

The location of the recharge zone, where cold seawater down-wells to initiate a hydrothermal circulation cell, also remains an open question with implications for heat and mass flow through MOR lithosphere. Early studies made a case for cross-axis fault-driven recharge at the EPR (15), while more recent studies propose that along-axis recharge zones drive a hydrothermal cell geometry that aligns with the strike of the axis (16–18). Others propose a hybrid model in which shallow flow along axis coalesces with deeper flow across-axis to drive fluid discharge directly within the AST (19). Nonetheless, all existing models for convective fluid flow geometry and location at fast-spreading ridges to date are constrained by the assumption that discharge sites are located on axis. Further, models for biological metapopulation connectivity at the EPR propose long-distance larval dispersal events as the mechanism that facilitates observed patterns of high regional gene flow and ecological succession (20). The presence of nearby off-axis vent sites would open the possibility for additional models of ecological succession dynamics for biological communities following catastrophic volcanic eruptions on axis.

Here, we report the discovery of an active high-temperature hydrothermal field outside of the AST at 9° 54′N EPR (6) (Fig. 1*A*). This spatially extensive site is currently the largest vent field known on the EPR between 9 and 10° N. This discovery documents the occurrence of active, high-temperature, off-axis hydrothermal venting on a fast-spreading MOR. Our finding has implications for understanding the heat and chemical budgets along the EPR spreading center and the ecological and evolutionary dynamics of benthic hydrothermal vent ecosystems.

Results and Discussion

Geology of the YBW-Sentry Vent Field. The EPR axis between 9° 26′N and 9° 51′N contains an AST, a continuous narrow cleft (~50 to 200 m wide) that strikes ~350°, with minor offsets and structural variations detected in near-bottom sonar surveys (6, 21–23). The AST is wider in the south and narrower and more structurally defined by faulting in the north, with collapsed margins defining its limits (21). North of 9° 51′N, the AST continues as a series of narrow, *en échelon* fissures superimposed on a summit area that is ~400 m wide near 9° 52′N and narrows to ~200 m wide at 9° 54′N. Based on autonomous underwater vehicle (AUV) *Sentry* 1-m resolution near-bottom bathymetric data, the EPR axis from ~9° 53′ to 57′N consists of small (~50 to 150 m wide, <10 m tall) constructional mounds along the current axis (24). The axis and volcanic mounds are extensively cut by fissures ~5 to 30 m wide.

Between 9° 52.4′N and 55.7′N, a prominent inferred nascent rift marked by fissures has developed ~300 to 600 m east of the current axis, with an orientation that parallels the axial trend (Fig. 1*B*). This rift is bilaterally symmetric, ~300 m wide, and rises from the surrounding seafloor at ~2,560 m depth with a relief of 10 m. The rift is defined by anastomosing ~5-m-wide *en échelon* off-axis fissures, which likely were the source of lava during the most recent eruption in 2005 and 2006, while the main EPR axis at this latitude did not erupt at that time (24). This putative rift provides evidence for volcanic activity east of the current EPR axis that may be active on long timescales ranging from ~100 y to <1 ky based on the spreading rate of 55 mm/y (25).

The YBW-Sentry vent field is located at 9° 54.3382′N, 104° 17.6711′W, 265 m east of this nascent rift, and ~750 m east of the EPR axis. The field is adjacent to a normal fault scarp with ~14 m vertical relief located 70 m to the east. The prominent sulfide spires that characterize this vent field were identified in near-bottom bathymetric data from AUV *Sentry* in 2019 during cruise AT42-21, but no direct seafloor observations were made at that time. The field was confirmed to be active and discovered in 2021 during cruise RR2102 and is named for the engineers who pioneered AUV technology development at Woods Hole Oceanographic Institution, Dana Yoerger, Albert Bradley, and Barrie Walden, and AUV *Sentry* (*SI Appendix*).

Based on observations made during the traverse from the current axis by remotely operated vehicle (ROV) *Jason* on dive 1322, there is a broad area of collapsed lobate and sheet flows and a large lava lake that extends northeast across the flanking crestal terrain, all of which were likely emplaced during the 2005 to 2006 eruptions (26, 27). At ~250 m east of the nascent rift, there is a transition from volcanic sheet and lobate flows to lobate lavas covered with orange to yellow hydrothermal sediment and hydrothermal rubble derived from toppled chimneys. The hydrothermal sediment is likely only ~5 to 20 cm thick since it only partially blankets the extrusive morphology. Fresh volcanic flows transition to hydrothermally coated lava with diffuse hydrothermal venting over a few tens of meters near the YBW-Sentry vent field. Diffuse vent fluids (4 to 43 °C) are expelled from microbial mat-lined cracks in the lava surface. Abundant, closely spaced hydrothermal chimlets (<0.5 m tall) are located on the field's periphery and grade into many densely spaced, much larger hydrothermal chimney structures.

The YBW-Sentry vent field is characterized by multiple sites of active high-temperature venting from more than 20 composite candelabra-type chimney structures (~5 to 10 m tall) built upon broad hydrothermal mounds. Vent chimneys, active and extinct, are arranged in an ~120-m-long, 35-m-wide construct trending ~350°, parallel to the adjacent fault scarp and AST. The widest part of the field is ~60 m across, with an estimated total area of ~5,500 m^2 and a volume of ~2,710 to 5,630 m^3 (*Materials and Methods*). The tallest vent chimneys in the central mound are ~10 m high. Individual chimneys stem from coalesced bases that can be several meters wide but commonly bifurcate into candelabra-like structures with individual spires typically <0.5 m in diameter. Many of the chimneys are capped by diffusive beehive structures.

Vent Fluid Compositions. A black smoker venting fluid at 368 °C was sampled from the YBW-Sentry vent field at the southwest corner of the central mound (Fig. 1 *C* and *D* and *SI Appendix*, Fig. S1 *A* and *B*), at a water depth of 2,555 m. Replicate fluids are Mg poor and acidic, with a pH (25 °C, 1 bar) of 3.3 (Table 1), characteristic of fluid–rock reaction with unsedimented basalt at high temperature (28). The high-temperature source fluid has an endmember Cl abundance of 518 mmol/kg, which is 4% lower than that of seawater (*SI Appendix* for endmember calculation details). Due to charge balance constraints, the Cl content sets the total cation abundance in the YBW-Sentry fluid. Along with absolute concentration assessments, molar ratios to Cl are useful for determining losses or gains in each element relative to the starting seawater composition. The

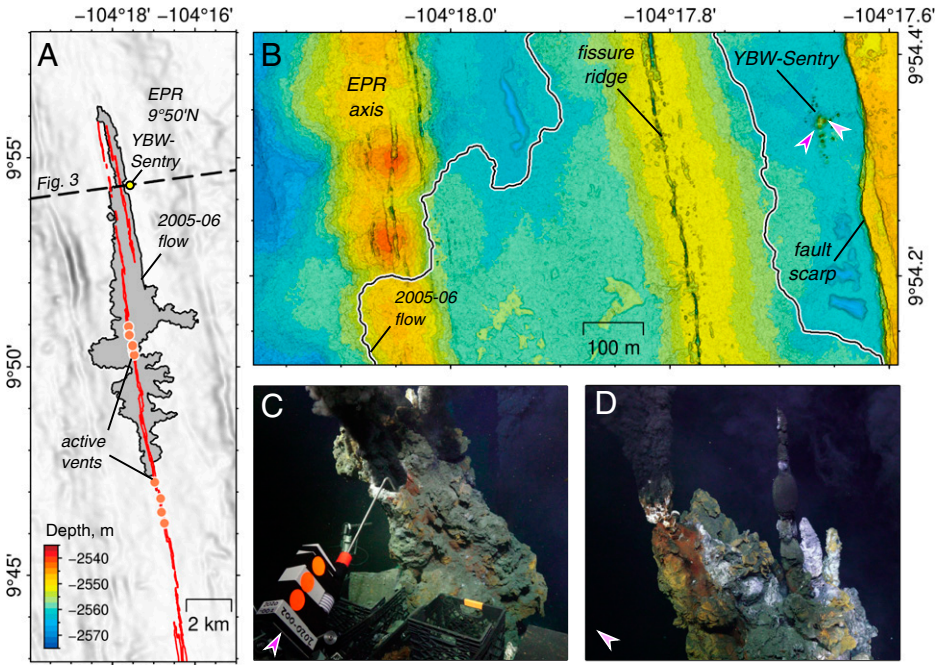

Fig. 1. (*A*) YBW-Sentry hydrothermal vent field (yellow dot), located ~750 m east of the EPR axial summit trough (red lines), ~5 to 7 km north of other known vents (orange dots). Gray polygon is 2005 to 2006 lava flow extent (24); dashed line is profile shown in Fig. 3. (*B*) Near-bottom bathymetric data (24) showing YBW-Sentry field, EPR axis, off-axis fissures, fault scarp, and 2005 to 2006 eruption extent (black line). (*C* and *D*) Photographs of actively venting sulfide chimneys at YBW-Sentry field, collected using cameras mounted on ROV *Jason*. Field of view is ~1 m wide and ~2 m wide at the center of the frame for *C* and *D*, respectively; positions of images and look directions are indicated by arrows in *B*.

depletion in Cl relative to seawater identifies YBW-Sentry as a vapor phase fluid. The fluid chemistry is consistent with formation via phase separation of a fluid with seawater Cl abundance at temperatures equal to or exceeding 391 °C, the two-phase boundary of seawater at the seafloor, followed by conductive cooling during ascent (29). Fluid compositions at Biovent, M, Bio9, and P, four on-axis vent sites located ~5 to 7 km south of YBW-Sentry (Fig. 1*A*), have been well studied since 1991 to 1994 (7, 28, 30) and provide useful context. Biovent and Bio9 consistently expelled vapor phase fluids throughout the 1991 to 2007 time series presented here, while M and P vent fluids have fluctuated between vapor phase compositions and brine phase fluids containing near-seawater Cl abundances (*SI Appendix*, Tables S1 and S2; vent locations tabulated in ref. 24).

The solubilities of the two most abundant transition metals in hydrothermal fluids, Fe and Mn, follow predictable temperature-dependent trends within basalt-hosted hydrothermal systems (31, 32). Thus, an empirical geothermometer can be used to infer the origin temperature of a fluid based on its Fe/Mn value (32). Dissolved Fe and Mn abundances at YBW-Sentry vent are 5.75 mmol/kg and 665 μmol/kg, respectively. Therefore, the dissolved Fe/Mn ratio of 8.65 points to a minimum estimated origin temperature of 437 ± 11 °C for YBW-Sentry vent fluid. The YBW-Sentry Fe/Cl value of 11×10^{3} and Mn/Cl value of 1.3×10^{-3} are similar to values at P, Bio9, and M during noneruptive periods (1993 to 2004 and 2007; Fig. 2*A*), indicating that metal supply to the fluids is not limited by rock availability. Further, other elements controlled by water–rock reactions, including the alkali metals K, Li, and Rb, are all enriched in the fluid relative to seawater, with endmember abundances of 19.2 mmol/kg, 387 μmol/kg, and 8.78 μmol/kg, respectively (Table 1). Likewise, the alkaline earth metals Ca, Sr, and Ba are also enriched in the fluid relative to seawater with endmember abundances of 25.1 mmol/kg, 103 μmol/kg, and 17.1 μmol/kg, respectively. YBW-Sentry vent K/Cl and Li/Cl ratios are consistent with those observed at P, Bio9, M, and Biovent during steady-state periods between eruptions (Fig. 2*B*), as are the Na/Cl and Ca/Cl ratios (*SI Appendix*, Fig. S2), demonstrating that there are sufficient water–rock reactions taking place to provide a source of Fe and Mn to the YBW-Sentry fluid. Dissolved Mn does not readily form sulfide minerals and is, therefore, less sensitive to cooling during fluid ascent than Fe. Any formation of Fe sulfide minerals after high-temperature equilibration during fluid up-flow would act to lower the Fe/Mn ratio, resulting in a lower estimated origin temperature. The estimated origin temperature of 437 ± 11 °C suggests that the off-axis YBW-Sentry vent fluid formed at a higher temperature than any other on-axis EPR vent observed and sampled during the 30-y on-axis time series between 9° 50.2787′N and 9° 50.9627′N. Origin temperatures for on-axis vent fluids were determined for samples collected during noneruptive periods (1993 to 2004 and 2007) using the Fe/Mn geothermometer (32) and for eruptive periods (1991 to 1992 and 2006) using Cl and Si geothermobarometry (*SI Appendix* for calculation details). The YBW-Sentry origin temperature exceeds the highest inferred origin temperature of an on-axis vapor phase vent by 12 °C and a brine phase vent by 10 °C (425 °C origin of Bio9 in 2007 and 427 °C origin of M vent in 2002, respectively; Fig. 2*C*).

The YBW-Sentry fluid Cl content, phase separation constraints, and the origin temperature estimate were used as parameters in a geothermobarometric model to infer an origin pressure of 379 ± 30 bar (Fig. 2*C*). The error estimate on pressure is based on the ±11 °C error on the Fe/Mn geothermometer (32). This calculation assumes the starting fluid contained a NaCl content equivalent to seawater, that the low-Cl vapor phase fluid did not mix with any other fluids, and that it rose to the seafloor following a single phase separation event without undergoing any additional episodes of phase separation. As observed at other basalt-hosted hydrothermal vents (23), the

Table 1. Endmember composition of YBW-Sentry vent

	YBW-Sentry*	Seawater
T_{max}, °C	368	2
pH, 25 °C, 1 bar	3.3	7.7
Na, mmol/kg	435	464
Cl, mmol/kg	518	540
Ca, mmol/kg	25.1	9.95
K, mmol/kg	19.2	10.1
SiO_2, mmol/kg	14.3	0.155
Li, µmol/kg	387	26
Rb, µmol/kg	8.78	1.23
Cs, nmol/kg	58.6	0
SO_4, mmol/kg	1.46	28.2
Br, µmol/kg	810	840
Sr, µmol/kg	103	87
Ba, µmol/kg	17.1	0.135
Fe, mmol/kg	5.75	0
Mn, µmol/kg	665	0
Cu, µmol/kg†	—‡	0
Zn, µmol/kg	38.0	0
Pb, nmol/kg	50.1	0
B, µmol/kg	366	398
Cr, nmol/kg†	—	0
Co, nmol/kg	901	0
Al, µmol/kg†	—	0
Cd, nmol/kg†	—	0
ΣH_2S, mmol/L	6.69	0
Na/Cl	0.84	0.86
K/Cl	0.037	0.019
K/Na	0.044	0.022
Ca/Cl	0.048	0.018
Sr/Cl, $\times 10^{-3}$	0.20	0.16
Li/Cl, $\times 10^{-3}$	0.75	0.05
Rb/Cl, $\times 10^{-3}$	0.017	0.002
Br/Cl, $\times 10^{3}$	1.56	1.56
B/Cl, $\times 10^{-3}$	0.71	0.74
Fe/Cl, $\times 10^{3}$	11	<0.00001
Mn/Cl, $\times 10^{-3}$	1.3	<0.00001
Fe/Mn	8.65	—
Fe/ΣH_2S	0.859	—
Sr/Ca	4.1	8.7

*Endmember fluid compositions were determined assuming no Mg in the source vent fluid and using the tabulated seawater composition.
†*SI Appendix*, Table S3 includes discrete measurements.
‡Not determined.

YBW-Sentry source fluid is significantly enriched in dissolved SiO_2 relative to seawater, with an endmember concentration of 14.3 mmol/kg. The SiO_2 content of the fluid indicates an origin pressure of 380 ±30 bar at 437 °C, a value consistent with the origin pressure estimated from its Cl abundance at the origin temperature indicated by the Fe/Mn geothermobarometer. The SiO_2 abundance for quartz saturation was determined by inputting the density of an equivalent NaCl solution (33) into a quartz solubility model (34). This inference assumes that the fluid's dissolved SiO_2 abundance is set by saturation with quartz and that there has been insignificant SiO_2 lost during fluid ascent to the seafloor. Formation of the YBW-Sentry fluid at 379 to 380 bar corresponds to a depth of 1.3 ± 0.3 km below the seafloor. This estimated origin depth is ~360 m deeper than inferred origin depths of on-axis vapor phase vents (e.g., 342 bar origin of Bio9 in 2007; Fig. 2*C*). Origin pressures for on-axis vent fluids were determined using either Cl or Si geothermobarometry (*SI Appendix* for calculation details). The composition of the single YBW-Sentry fluid is otherwise consistent with formation via high-temperature basalt–seawater reaction, as previously observed for circulating fluids expelled on axis at the EPR between 9° 46′N and 9° 51′N over the last 30 y (28).

Controls on Vent Fluid Flow Path Geometry. Geothermobarometric calculations combined with a depth-migrated seismic reflection image indicate that fluids at YBW-Sentry originate at ~160 m above the top of the axial magma lens (AML), which is ~1.45 km deep (35) (Fig. 3 *A* and *B*). In contrast, the vapor phase fluids at on-axis vents Bio9 and P originate at shallower depths, ≥490 m above the magma lens, while the brine phase fluids at M vent originate at similar depths. The seismic reflection data show that the AML near YBW-Sentry consists of two distinct reflections, the eastern of which is slightly deeper (AML 2; Fig. 3*B*). YBW-Sentry is located above the eastern edge of this eastern AML, which consists of a 700-m-wide, moderate-amplitude, west-dipping double reflection. The western AML is a single, flat, high-amplitude reflection event that is ~850 m wide and is offset west from YBW-Sentry (Fig. 3*B*). Using the seismic reflection data and near-bottom multibeam data (end points of the dashed line in Fig. 3*B*), we estimate a fault dip angle of ~72°. The downward-projected seafloor scarp of the fault east of YBW-Sentry shows that it is plausible that the fault damage zone could intersect with the eastern edge of the brighter AML reflection (Fig. 3*B*). The observation of deep fluid circulation at YBW-Sentry supports assertions of a thin impermeable thermal boundary layer (i.e., 2 to 20 m thick) (36) that separates the base of a hydrothermal circulation cell from the underlying magma body in this off-axis setting. Hydrothermal fluids that undergo reaction near the top of the magma lens have also been inferred at the Solwara 1 deposit in the East Manus Basin (Bismarck Sea, southwestern Pacific) by inverse modeling of near-seafloor magnetic data (37). Our results suggest that the permeability structure controlling YBW-Sentry fluid flow path geometry is fundamentally different from what is inferred to occur in the floor of the axial summit trough at 9° 50′N EPR, where dike injection and subsequent cooling create vertical fluid migration pathways that focus hydrothermal fluid circulation within the topographic axis (6).

The 9° 26′N to 51′N segment of the EPR is considered to represent a buoyancy-dominated ridge crest, where plate separation and asthenospheric upwelling are accommodated via magmatic accretion by diking sourced from a continuously replenished magma lens (38). However, the location of the YBW-Sentry vent field indicates that it is a fault-controlled hydrothermal system, despite its geographic setting on a fast-spreading ridge. In planform, chimneys in the YBW-Sentry vent field trend parallel to an inward-dipping normal fault scarp (Fig. 3*A*), indicating that fluid pathways could be controlled by the enhanced permeability created by tectonic-driven fracturing along the fault plane. A sharp increase in effective permeability of one to three orders of magnitude occurs at the boundary between the extrusive pillow basalts and intrusive sheeted dikes, termed the crustal layer 2A/2B boundary, in hydrothermal discharge zones (39). On axis at 9° 51.3 to 56.2′N EPR, the layer 2A/2B boundary occurs at an average depth of ~130 ± 15 m below seafloor (35) (Fig. 3*B*). Considering the vent field location with respect to crustal structure and the extrapolated fault plane orientation (Fig. 3 *A* and *B*), the YBW-Sentry fluids reach their maximum depth just above the AML in layer 2B. The permeability ratio between layer 2B and the fault plane is low and apparently constrains the rising fluid flow path to the fault zone. When the ascending fluids reach the layer 2A/2B boundary, the permeability ratio between layer 2A

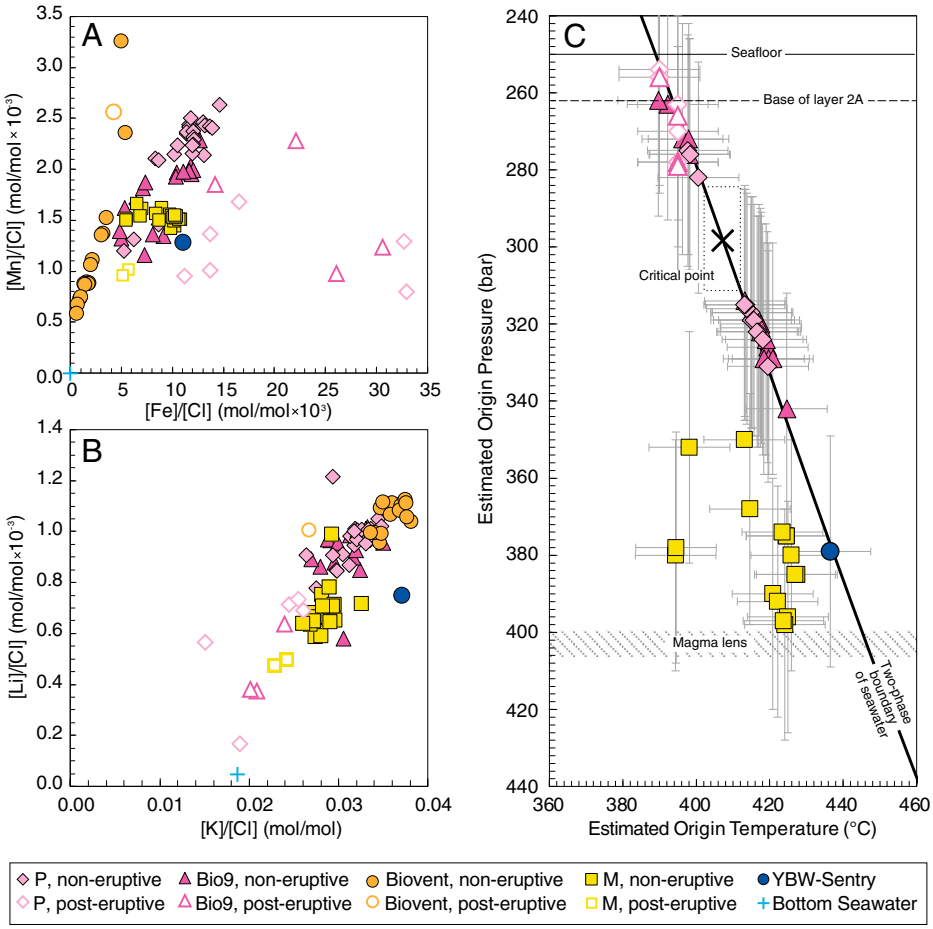

Fig. 2. (*A* and *B*) YBW-Sentry fluid composition compared with on-axis vent compositions from 1991 to 2007 for (*A*) endmember Mn/Cl versus Fe/Cl and (*B*) endmember Li/Cl versus K/Cl. (*C*) Estimated origin pressure versus estimated origin temperature for vent fluids, relative to the seafloor (thin solid black line), base of layer 2A (dashed line), magma lens depth, two-phase boundary of seawater (thick solid black line), and critical point (black ×) (29). Origin conditions were not estimated in the region ±5 °C of the critical point (dotted box). Errors (2σ) are indicated with gray error bars.

and the fault plane increases. The fluid then departs from the fault plane at this leakage depth (Fig. 3*B*) to rise vertically to the seafloor through higher-permeability features in layer 2A, such as crack and fissure networks. These features may be vertical or antithetic to the main fault.

Extensional fault-controlled hydrothermal flow is frequently invoked to explain the location and local geometry of black smoker vent fields at intermediate- and slow-spreading ridges, such as Main Endeavor (40) and Mothra (41) on the central-southern portion of the Endeavor Segment of the Juan de Fuca Ridge and TAG (42) and Logatchev (43) on the Mid-Atlantic Ridge. For example, the locations of the Main Endeavor field (MEF) and Mothra hydrothermal field are considered to be primarily controlled by a bounding fault that defines the western edge of the valley wall (40, 41). At MEF, black smoker hydrothermal vents are aligned along strike, up to 100 m east of this western boundary fault. The largest, most active sulfide structures are located either on or adjacent to intersections of ridge-parallel faults and fissures east of the western wall bounding fault (e.g., Hulk and Dante vent sites) (40). Episodic extension-driven fault motion is theorized to maintain zones of high permeability that constrain fluid flow and vent field location at Mothra (e.g., Twin Peaks, Faulty Tower, and Crab Basin vent sites) (41). Fault-associated hydrothermal activity is also observed in tectonic windows that show evidence of alteration of subaxial fault zones by ancient high-temperature fluids (44).

In contrast, fault-controlled hydrothermal flow is rarely observed at the seafloor in fast-spreading centers. Many on-axis black smokers at the well-studied 9° 50′N EPR system are located above primary fissures and dikes, including Bio9, P vent, and Biovent. Their location in the floor of the AST makes the vent fluids sensitive to crustal permeability changes and temporally variable heat sourced from seafloor eruptions and associated dike intrusions (28). Highly dynamic conditions drive shifts in the maximum depth of fluid circulation on short timescales of months to years. These changes to maximum fluid depth are primarily responsible for the iconic high spatial and temporal variability in source fluid Cl and cation content that is well recognized at 9° 50′N EPR (28, 30). This vent type is widely associated with fast-spreading centers. However, a few vents at 9° 50′N EPR are located along the AST walls, including M and Q. The more-episodic nature of active venting at M and Q vents (45) suggests that fluid flow pathways are more complex at these sites. M vent and Q vent may represent a second type of fast-spreading ridge hydrothermal field controlled by faulting and diking processes. Hence the off-axis YBW-Sentry vent represents a third type of fast-spreading ridge-hosted hydrothermal system that is tectonically controlled.

Benthic Macrofaunal Observations. Benthic fauna documented in ROV imagery of the YBW-Sentry vent field belong to seven phyla distributed across four habitat zones: focused

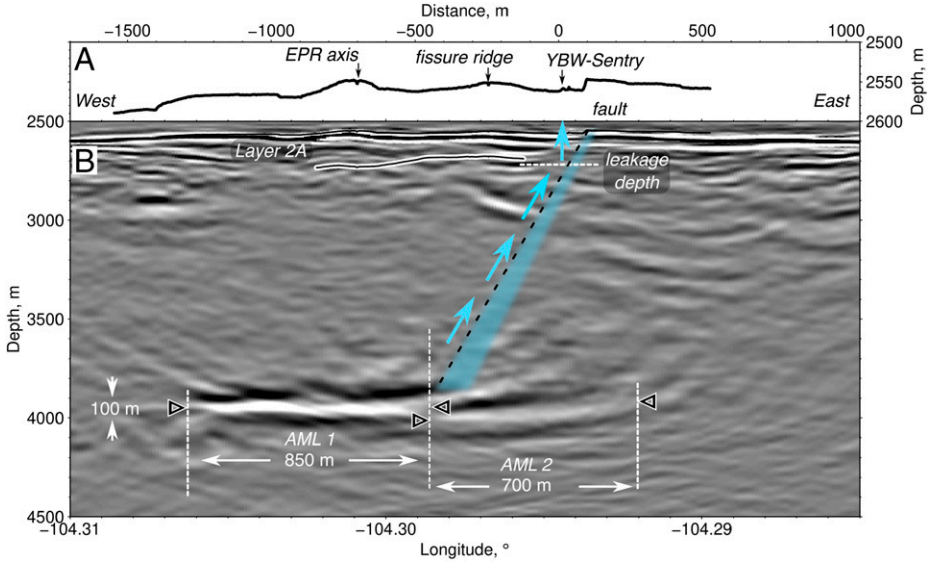

Fig. 3. (*A*) Bathymetric profile across the YBW-Sentry vent field at the location shown in Fig. 1. (*B*) Depth-migrated seismic reflection ridge-perpendicular 2D profile crossing the location of YBW-Sentry showing the presence of axial magma lenses (AML 1 and AML 2). Open triangles mark AML reflections. Black dashed line with blue shading is the inferred fault damage zone, projected into the subsurface, based on the dip of the scarp at the seafloor derived from AUV Sentry multibeam data. Black/white line is the base of layer 2A extrapolated from an on-axis study (35). Blue arrows mark the possible fluid pathway along the fault to the 2A/2B boundary, termed the leakage depth. Fluids depart from the fault plane at the leakage depth to ascend vertically through layer 2A.

fluid flow, diffuse flow, inactive sulfide deposits, and peripheral basalt (*SI Appendix*, Fig. S3). Alvinellid worms were observed on active black smoker walls and beehives (*SI Appendix*, Fig. S3 *A* and *B*). Diffuse-flow areas hosted polynoid scale worms, limpets, serpulid worms, nereidid worms, amphipods, and bythograeid crabs (*SI Appendix*, Fig. S3 *C* and *D*). Sulfide deposits hosted cladorhizid sponges and serpulid worms (*SI Appendix*, Fig. S3 *E* and *F*) and were covered by iron staining and fuzzy white microbial mats (*SI Appendix*, Fig. S3*G*). Finally, a bamboo octocoral, three *Relicanthus daphneae* anemones, comatulid crinoids, sea cucumbers, brittle stars, and serpulid worms were observed on the peripheral basalt areas (*SI Appendix*, Fig. S3*H*). The presence of an ∼30-cm-tall bamboo octocoral on peripheral basalt in the vicinity of YBW-Sentry suggests that this area was not completely paved over by lava flows during the 2005 to 2006 eruptions. Estimates of axial growth rate in deep-sea bamboo corals range between 0.1 and 2.3 cm/y (46), so this individual could be 10 to 300 y old. The biological community at YBW-Sentry appears similar to those associated with active on-axis Q vent, L Hot 8, L vent, P vent, BioVent, and M vent and the off-axis, inactive Lucky's Mound and Sentry Spire fields (*SI Appendix* for further details and locations). Off-axis, active vent fields such as YBW-Sentry may also host rare or habitat-endemic species (47). Furthermore, sites like YBW-Sentry could supply recolonizing larvae to repopulate on-axis vents after catastrophic eruptions and thus influence succession and evolutionary dynamics.

Implications

The discovery of the YBW-Sentry hydrothermal field provides additional insight into the fundamental controls on hydrothermal vent location along fast-spreading midocean ridges. Vent location is not strictly magmatically controlled beneath the bathymetric axis, and it is not restricted to the AST. Instead, local vent geometry spans a spectrum from magmatically controlled sites in the floor of the AST (e.g., Bio9, P, and Biovent), to sites along the walls of the AST that are controlled by coupled influences of diking and tectonics (e.g., M and Q), to off-axis sites that are tectonically controlled (YBW-Sentry).

The YBW-Sentry active sulfide deposit is spatially extensive, covering roughly twice the area of any single known active sulfide field on the EPR axis between 9° and 10° N. Assuming that the deposition rates of sulfide minerals are similar in on- and off-axis settings along 9° to 10° N EPR, YBW-Sentry likely existed throughout the last three decades since the discovery of vents in the EPR 9° 50′N area in 1989 (7). Furthermore, relative to historical trends in circulation depth inferred from the geochemistry of on-axis vents at 9° 50′N EPR, YBW-Sentry fluids percolate to greater depths in the oceanic crust. This tectonically controlled vent field may thus experience long-term stability in fluid temperature and composition, in stark contrast to the highly dynamic conditions that have long been associated with dike-controlled, on-axis vents along fast-spreading MORs.

The 2005 to 2006 eruptions of new lava between 9° 47′N and 9° 56′N EPR were fatal to many benthic macrofaunal communities. A shift in species composition was observed in both larvae and colonists at disturbed sites (20). A proposed mechanism for this change involves the successful colonization by highly dispersive larvae from remote populations (more than 300 km away) that capitalized upon low local larval supply and therefore less competition. The discovery of the nearby YBW-Sentry vent field suggests that posteruption colonizers of fast-spreading systems could also be sourced by more local off-axis systems that may have greater temporal stability.

The distance over which high-temperature convective circulation cells extend off axis must be revised for fast-spreading centers. Off-axis high-temperature vents on fast-spreading MORs constitute previously unaccounted for sources of heat and chemicals that must be incorporated into global ocean budget models. Systematic AUV mapping of off-axis regions is needed to understand the distribution, frequency, and physical controls on active off-axis vent fields. This understanding is necessary to determine their contribution to heat and chemical fluxes and role in metacommunity dynamics on broad scales.

Materials and Methods

YBW-Sentry Vent Fluid Sample Collection. Approximately 6 h were spent exploring the YBW-Sentry hydrothermal field during ROV *Jason* dive 1322 on cruise RR2102 aboard R/V *Roger Revelle* from 18 to 19 April 2021 (coordinated universal time [UTC]). Vent fluid samples were collected with a pair of 755-mL titanium syringe-style majors samplers (48) with ROV *Jason* during the R/V *Roger Revelle* cruise RR2102 on 18 April 2021 (UTC). Before deployment, each majors sampler was cleaned with Milli-Q water, followed by high-performance liquid chromatography grade acetone, methyl tert-butyl ether, and hexane, in succession. The maximum temperature was recorded using a National Institute of Standards and Technology (NIST)-standardized thermocouple aligned with the snorkel inlet tips. Samples were extracted and processed immediately following ROV recovery.

YBW-Sentry Vent Fluid Analytical Geochemistry Methods. Fluid pH (25 °C, 1 atm) aliquots were drawn first for shipboard analysis. Dissolved ΣH_2S aliquots were drawn into gastight syringes. Aliquots for other dissolved species (Li, B, Na, Mg, Al, SiO_2, SO_4, Cl, K, Ca, Cr, Mn, Fe, Co, Cu, Zn, Br, Rb, Sr, Cd, Ba, Pb) were transferred to acid-washed high-density polyethylene (HDPE) Nalgene bottles and stored at room temperature before shore-based analysis. Aliquots for trace elements and transition metal analysis were acidified to a pH less than 2 with concentrated Optima HCl. Aliquots for aqueous SiO_2 determination were diluted 100-fold (vol/vol) with ultrapure Milli-Q water in HDPE Nalgene bottles. After each sampler was drained of fluid, the "dregs" (e.g., solid precipitates) were collected on a 0.2-μm filter by rinsing the inner chamber with Milli-Q water. The filters were stored dry.

The abundance of chemical species measured at sea is reported in units of mmol/L fluid, while species measured onshore are reported in units of nmol/kg, μmol/kg, or mmol/kg fluid. Vent fluid pH (25 °C, 1 atm) was measured by potentiometry using a Fisherbrand accuTupH™ combination Ag/AgCl electrode calibrated with pH 4 and 7 buffers. Bottom seawater pH was calibrated with pH 7 and 10 buffers and otherwise measured similarly. The majors samplers are not gastight, and thus reported ΣH_2S abundances are minima (ΣH_2S_{min}). Dissolved ΣH_2S_{min} samples were precipitated as $Ag_2S_{(s)}$ in $AgNO_3$ solution in glass vials for shore-based gravimetric abundance determination following filtration onto 0.2-μm filters. Dissolved major species concentrations were determined onshore via ion chromatography (IC) (Mg, SO_4, Cl, K, Ca, Br) at Lehigh University. Precipitates can form within the titanium sampler before sample retrieval and during storage of the HDPE bottle containing the acidified aqueous aliquot. These two precipitate fractions, termed the dregs and bottle filter fractions, each underwent complete acid digestion at 80 °C in Teflon Savillex vials in the shore-based laboratory using Optima reverse aqua regia (49). Trace elements and transition metals were determined onshore via inductively coupled plasma mass spectrometry (ICP-MS) (Li, B, Na, Al, Cr, Mn, Fe, Co, Cu, Zn, Rb, Sr, Cd, Ba, Pb) at Woods Hole Oceanographic Institution. Separate analyses of the digested dregs, digested bottle filter particulates, and aqueous samples were mathematically recombined to produce a total budget for each species in each discrete fluid sample. Dissolved SiO_2 abundances were determined via colorimetry (30). NIST-traceable external standards bracketed all samples determined via IC, ICP-MS, and colorimetry. Analytical uncertainties (2s) were ±0.05 units for pH (25 °C, 1 atm); ±10% for ΣH_2S and Br; ±3% for Li, Na, Mg, SiO_2, SO_4, Cl, K, Ca, Mn, Fe, and Sr; and ±5% for B, Al, Cr, Co, Cu, Zn, Rb, Cd, Ba, and Pb.

Biovent, M, Bio 9, P Vent Fluid Sample Collection, and Analytical Geochemistry Methods. The sampling approach and analytical methods for time series vent fluids are described in refs. 28, 30, 48, and 50–53.

Seismic Reflection Data. The seismic reflection two-dimensional (2D) profile shown in Fig. 3 is extracted from the three-dimensional (3D) seismic volume collected in the summer of 2008 during R/V *M. G. Langseth* cruise MGL0812. Seismic data were collected with four 6-km-long streamers, each with 468 channels at 12.5 m group spacing and two 1,650-cubic-inch air-gun arrays. The preliminary reflection image focusing on the axial magma lenses along the ridge-perpendicular line crossing the YBW-Sentry vent field at 9° 54.3′N was obtained using the standard Kirchhoff prestack depth migration scheme and published velocity model (54, 55).

Vent Field Volumetric Estimate. The total volume of hydrothermal constructs and chimneys in the YBW-Sentry vent field was obtained using the 1-m resolution near-bottom bathymetric data collected by AUV *Sentry* by summing the volume of the material above a reference base level within a manually interpreted polygon encompassing all of the mapped chimney structures. Uncertainty was estimated by assuming minimum and maximum base levels of 2,560 and 2,561 m, respectively. Calculations were performed using the Generic Mapping Tools, v6 (56).

Data Availability. The seismic dataset collected in 2008 is archived in the Interdisciplinary Earth Data Alliance (IEDA) Marine Geoscience Data System (MGDS) (54). The near-bottom multibeam data are archived in IEDA MGDS (57). All other study data are included in this article and/or *SI Appendix*. Previously published data were used for this work (28).

ACKNOWLEDGMENTS. Financial support was provided by the NSF Awards OCE-1949938 (to J.M.M.), OCE-1948936 (to R.P.-T.), and OCE-1949485 (to D.J.F. and T.B.). We thank the captain, officers, and crew of the R/V *Revelle* and the ROV *Jason* group for their expertise at sea during RR2102. We are grateful to Karen L. Von Damm and her laboratory members for collecting the legacy on-axis vent fluid chemistry dataset. We acknowledge John Jamieson for his thoughtful comments. We also thank Linda McDermott, Liliana Monroy, and Mauricio Herrera for their support. We are grateful to the editor, reviewer Jeffrey Karson, and one anonymous reviewer for providing helpful suggestions that improved the manuscript.

Author affiliations: [a]Department of Earth and Environmental Sciences, Lehigh University, Bethlehem, PA 18015; [b]Institute of Geophysics and Planetary Physics, Scripps Institution of Oceanography, University of California, San Diego, CA 92037; [c]Department of Earth Science–Centre for Deep Sea Research, University of Bergen, N-5007 Bergen, Norway; [d]Department of Biological Sciences, Lehigh University, Bethlehem, PA 18015; [e]Institut de Physique du Globe de Paris, CNRS, 75005 Paris, France; and [f]Department of Geology and Geophysics, Woods Hole Oceanographic Institution, Woods Hole, MA 02543

1. H. Elderfield, A. Schultz, Mid-ocean ridge hydrothermal fluxes and the chemical composition of the ocean. *Annu. Rev. Earth Planet. Sci.* **24**, 191–224 (1996).
2. N. LeBris *et al.*, Hydrothermal energy transfer and organic carbon production at the deep seafloor. *Front. Mar. Sci.* **5**, 1–24 (2019).
3. G. J. Dick, The microbiomes of deep-sea hydrothermal vents: Distributed globally, shaped locally. *Nat. Rev. Microbiol.* **17**, 271–283 (2019).
4. F. N. Spiess *et al.*, East Pacific Rise: Hot springs and geophysical experiments. *Science* **207**, 1421–1433 (1980).
5. D. J. Fornari, R. W. Embley, *Seafloor Hydrothermal Systems: Physical, Chemical, Biological, and Geochemical Interactions*, S. E. Humphris, Ed. (*Geophysical Monograph*, American Geophysical Union, Washington, DC, 1995).
6. D. Fornari, M. Tivey, H. Schouten, "Submarine lava flow emplacement at the East Pacific rise 9° 50′N: Implications for uppermost ocean crust stratigraphy and hydrothermal fluid circulation" in *Mid-Ocean Ridges: Hydrothermal Interactions Between the Lithosphere and Oceans*, C. R. German, J. Lin, L. M. Parson, Eds. (Geophysical Monograph, American Geophysical Union, Washington, DC, 2004), pp. 187–218.
7. R. M. Haymon *et al.*, Hydrothermal vent distribution along the East Pacific Rise crest (9°09′-54′N) and its relationship to magmatic and tectonic processes on fast-spreading mid-ocean ridges. *Earth Planet. Sci. Lett.* **104**, 513–534 (1991).
8. R. M. Haymon, S. M. White, Fine-scale segmentation of volcanic/hydrothermal systems along fast-spreading ridge crests. *Earth Planet. Sci. Lett.* **226**, 367–382 (2004).
9. M. Harris *et al.*, Hydrothermal cooling of the ocean crust: Insights from ODP Hole 1256D. *Earth Planet. Sci. Lett.* **462**, 110–121 (2017).
10. R. M. Haymon, K. C. Macdonald, S. B. Benjamin, C. J. Ehrhardt, Manifestations of hydrothermal discharge from young abyssal hills on the fast-spreading East Pacific Rise flank. *Geology* **33**, 153–156 (2005).
11. F. J. Fontaine, W. S. D. Wilcock, D. A. Butterfield, Physical controls on the salinity of mid-ocean ridge hydrothermal vent fluids. *Earth Planet. Sci. Lett.* **257**, 132–145 (2007).
12. A. Nicolas, D. Mainprice, F. Boudier, High-temperature seawater circulation throughout crust of oceanic ridges: A model derived from the Oman ophiolites. *J. Geophys. Res.* **108**, 1–20 (2003).
13. C. A. Stein, S. Stein, A model for the global variation in oceanic depth and heatflow with lithospheric age. *Nature* **359**, 123–128 (1992).
14. J. Maclennan, T. Hulme, S. C. Singh, Thermal models of oceanic crustal accretion: Linking geophysical, geological and petrological observations. *Geochem. Geophys. Geosyst.* **5**, Q02F25 (2004).
15. R. P. Lowell, P. A. Rona, R. P. Von Herzen, Seafloor hydrothermal systems. *J. Geophys. Res. Solid Earth* **100**, 327–352 (1995).
16. M. Tolstoy, F. Waldhauser, D. R. Bohnenstiehl, R. T. Weekly, W. Y. Kim, Seismic identification of along-axis hydrothermal flow on the East Pacific Rise. *Nature* **451**, 181–184 (2008).
17. M. Marjanović, N. Fuji, S. C. Singh, T. Belahi, J. Escartín, Seismic signatures of hydrothermal pathways along the East Pacific Rise between 9°16′ and 9°56′N. *J. Geophys. Res. Solid Earth* **122**, 10,241–10,262 (2017).

18. F. Waldhauser, M. Tolstoy, Seismogenic structure and processes associated with magma inflation and hydrothermal circulation beneath the East Pacific Rise at 9°50′N. *Geochem. Geophys. Geosyst.* **12**, Q08T10 (2011).
19. J. Hasenclever *et al.*, Hybrid shallow on-axis and deep off-axis hydrothermal circulation at fast-spreading ridges. *Nature* **508**, 508–512 (2014).
20. L. S. Mullineaux, D. K. Adams, S. W. Mills, S. E. Beaulieu, Larvae from afar colonize deep-sea hydrothermal vents after a catastrophic eruption. *Proc. Natl. Acad. Sci. U.S.A.* **107**, 7829–7834 (2010).
21. D. J. Fornari, R. M. Haymon, M. R. Perfit, T. K. P. Gregg, M. H. Edwards, Axial summit trough of the East Pacific Rise 9°-10°N: Geological characteristics and evolution of the axial zone on fast spreading mid-ocean ridges. *Geochem. Geophys. Geosyst.* **103**, 9827–9855 (1998).
22. S. A. Soule *et al.*, Channelized lava flows at the East Pacific Rise crest 9°-10°N: The importance of off-axis lava transport in developing the architecture of young oceanic crust. *Geochem. Geophys. Geosyst.* **6**, Q08005 (2005).
23. J. Escartín *et al.*, Interplay between faults and lava flows in construction of the upper oceanic crust: The East Pacific Rise crest 9°25′-9°58′N. *Geochem. Geophys. Geosyst.* **8**, Q06005, (2007).
24. J.-N. Wu *et al.*, Extent and volume of lava flows erupted at 9°50′N, East Pacific Rise in 2005–2006, using repeat near-bottom surveys. *Geochem. Geophys. Geosyst.* **23**, e2021GC010213 (2022).
25. S. Carbotte, K. Macdonald, East Pacific Rise 8°-10°30′N: Evolution of ridge segments and discontinuities from SeaMARC II and three-dimensional magnetic studies. *J. Geophys. Res.* **97**, 6959–6982 (1992).
26. S. A. Soule, D. J. Fornari, M. Perfit, K. H. Rubin, New insights into mid-ocean ridge volcanic processes from the 2005 – 2006 eruption of the East Pacific Rise, 9° 46′ N – 9° 56′N. *Geology* **35**, 1079–1082 (2007).
27. A. F. Fundis, S. A. Soule, D. J. Fornari, M. R. Perfit, Paving the seafloor: Volcanic emplacement processes during the 2005–06 eruption at the fast-spreading East Pacific Rise, 9°50′N. *Geochem. Geophys. Geosyst.* **11**, Q08024 (2010).
28. K. L. Von Damm, Evolution of the hydrothermal system at east pacific rise 9°50′N: Geochemical evidence for changes in the upper oceanic crust. *Geophys. Monogr.* **148**, 285–304 (2004).
29. J. L. Bischoff, R. J. Rosenbauer, Liquid-vapor relations in the critical region of the system NaCl-H_2O from 380 to 415°C: A refined determination of the critical point and two-phase boundary of seawater. *Geochim. Cosmochim. Acta* **52**, 2121–2126 (1988).
30. K. L. Von Damm, Chemistry of hydrothermal vent fluids from 9°–10°N, East Pacific Rise: "Time zero," the immediate posteruptive period. *J. Geophys. Res.* **105**, 11203 (2000).
31. N. J. Pester, K. Ding, W. E. Seyfried, Magmatic eruptions and iron volatility in deep-sea hydrothermal fluids. *Geology* **42**, 255–258 (2014).
32. N. J. Pester, M. Rough, K. Ding, W. E. Seyfried, A new Fe/Mn geothermometer for hydrothermal systems: Implications for high-salinity fluids at 13°N on the East Pacific Rise. *Geochim. Cosmochim. Acta* **75**, 7881–7892 (2011).
33. T. Driesner, C. A. Heinrich, The system H2O–NaCl. Part I: Correlation formulae for phase relations in temperature–pressure–composition space from 0 to 1000°C, 0 to 5000bar, and 0 to 1 XNaCl. *Geochim. Cosmochim. Acta* **71**, 4880–4901 (2007).
34. K. L. Von Damm, J. L. Bischoff, R. J. Rosenbauer, Quartz solubility in hydrothermal seawater: An experimental study and equation describing quartz solubility for up to 0.5 M NaCl solutions. *Am. J. Sci.* **291**, 977–1007 (1991).
35. M. Marjanović *et al.*, Crustal magmatic system beneath the East Pacific Rise, (8°20′ to 10°10′N): Implications for tectonomagmatic segmentation and crustal melt transport at fast-spreading ridges. *Geochem. Geophys. Geosyst.* **19**, 4584–4611 (2018).
36. R. P. Lowell, L. N. Germanovich, Hydrothermal processes at mid-ocean ridges: Results from scale analysis and single-pass models. *Geophys. Monogr.* **148**, 219–244 (2004).
37. C. G. Galley, J. W. Jamieson, P. G. Lelièvre, C. G. Farquharson, J. M. Parianos, Magnetic imaging of subseafloor hydrothermal fluid circulation pathways. *Sci. Adv.* **6**, 1–11 (2020).
38. W. R. Buck, L. L. Lavier, A. N. B. Poliakov, Modes of faulting at mid-ocean ridges. *Nature* **434**, 719–723 (2005).
39. T. Barreyre, J.-A. Olive, T. J. Crone, R. A. Sohn, Depth-dependent permeability and heat output at basalt-hosted hydrothermal systems across mid-ocean ridge spreading rates. *Geochem. Geophys. Geosyst.* **19**, 1259–1281 (2018).
40. J. R. Delaney, V. Robigou, R. E. McDuff, M. K. Tivey, Geology of a vigorous hydrothermal system on the Endeavour segment, Juan de Fuca Ridge. *J. Geophys. Res. Solid Earth* **97**, 19663–19682 (1992).
41. D. A. Glickson, D. S. Kelley, J. R. Delaney, Geology and hydrothermal evolution of the Mothra hydrothermal field, Endeavour segment, Juan de Fuca Ridge. *Geochem. Geophys. Geosyst.* **8**, Q06010, (2007).
42. B. J. deMartin, R. A. Sohn, J. Pablo Canales, S. E. Humphris, Kinematics and geometry of active detachment faulting beneath the Trans-Atlantic Geotraverse (TAG) hydrothermal field on the Mid-Atlantic Ridge. *Geology* **35**, 711–714 (2007).
43. S. Petersen *et al.*, The geological setting of the ultramafic-hosted Logatchev hydrothermal field (14°45′N, Mid-Atlantic Ridge) and its influence on massive sulfide formation. *Lithos* **112**, 40–56 (2009).
44. N. W. Hayman, J. A. Karson, Crustal faults exposed in the Pito Deep Rift: Conduits for hydrothermal fluids on the southeast Pacific Rise. *Geochem. Geophys. Geosyst.* **10**, Q02013 (2009).
45. D. Fornari *et al.*, The East Pacific Rise between 9°N and 10°N: Twenty-five years of integrated, multidisciplinary oceanic spreading center studies. *Oceanography (Wash. DC)* **25**, 18–43 (2012).
46. L. Watling, S. C. France, E. Pante, A. Simpson, Biology of deep-water octocorals. *Adv. Mar. Biol.* **60**, 41–122 (2011).
47. S. Gollner *et al.*, Animal community dynamics at senescent and active vents at the 9°N East Pacific Rise after a volcanic eruption. *Front. Mar. Sci.* **6**, 832, 10.3389/fmars.2019.00832 (2020).
48. K. L. Von Damm *et al.*, Chemistry of submarine hydrothermal solutions at 21°N, East Pacific Rise. *Geochim. Cosmochim. Acta* **49**, 2197–2220 (1985).
49. J. M. McDermott, S. P. Sylva, S. Ono, C. R. German, J. S. Seewald, Geochemistry of fluids from Earth's deepest ridge-crest hot-springs: Piccard hydrothermal field, Mid-Cayman Rise. *Geochim. Cosmochim. Acta* **228**, 95–118 (2018).
50. J. Bryce, F. Prado, K. Von Damm, Vent Fluid Chemistry Data from Samples Acquired with HOV Alvin during Atlantis Expedition AT11-20 2004 at the East Pacific Rise 9N Site (IEDA, 2015). 10.15941/IEDA/317362. https://www.marine-geo.org/tools/search/Files.php?data_set_uid=17362#datasets (Accessed 4 March 2022).
51. J. Bryce, F. Prado, K. Von Damm, Vent Fluid Chemistry Data, Including Metals Fractions and Dissolved Majors, from Fluid Samples Acquired with HOV Alvin during Atlantis Expedition AT15-06 (2006) at the East Pacific Rise 9N Site (IEDA, 2015). 10.1594/IEDA/317365. https://www.marine-geo.org/tools/search/Files.php?data_set_uid=17365 (Accessed 4 March 2022).
52. J. Bryce, F. Prado, K. Von Damm, Vent Fluid Chemistry Data, Including Metals Fractions and Dissolved Majors, from Fluid Samples Acquired with HOV Alvin during Atlantis Expedition AT15-13 (2006) at the East Pacific Rise 9N Site (IEDA, 2015). 10.1594/IEDA/317364. https://www.marine-geo.org/tools/search/Files.php?data_set_uid=17364 (Accessed 4 March 2022).
53. J. Bryce, F. Prado, K. Von Damm, Vent Fluid Chemistry Data, Including Metals Fractions and Dissolved Majors, from Fluid Samples Acquired with HOV Alvin during Atlantis Expedition AT15-27 (2007) at the East Pacific Rise 9N Site (IEDA, 2015). 10.1594/IEDA/317603. https://www.marine-geo.org/tools/search/Files.php?data_set_uid=17603 (Accessed 4 March 2022).
54. J. Mutter, S. Carbotte, J. P. Canales, M. Nedimovic, Multi-Channel Seismic Shot Data from the East Padfic Rise 9 Degrees North Spreading Center Segment Acquired during RIV Marcus G. Langseth Expedition MGL0812 (2008) (IEDA, 2014). 10.1594/IEDA/314654. https://www.marine-geo.org/tools/search/Files.php?data_set_uid=14654 (Accessed 18 May 2021).
55. M. Marjanović, R.-É. Plessix, A. Stopin, S. C. Singh, Elastic versus acoustic 3D full waveform inversion at the East Pacific Rise 9°50′N. *Geophys. J. Int.* **216**, 1497–1506 (2019).
56. P. Wessel, W. H. F. Smith, R. Scharoo, J. Luis, F. Wobbe, Generic mapping tools: Improved version released. *Eos (Wash. DC)* **94**, 409–410 (2013).
57. R. Parnell-Turner, D. Fornari, J. McDermott, T. Barreyre, J.-N. Wu, Processed bathymetric data (netCDF grid) from 9°50′N, East Pacific Rise, acquired in 2018, 2019, and 2021 during AUV Sentry near-bottom dives (IEDA, 2021) 10.26022/IEDA/330373. https://www.marinegeo.org/tools/search/Files.php?data_set_uid=30373#datasets (Accessed 18 May 2021).